APPLIED SCIENCES AND ENGINEERING

Toward garnet electrolyte–based Li metal batteries: An ultrathin, highly effective, artificial solid-state electrolyte/metallic Li interface

Kun (Kelvin) Fu,[1,2]* Yunhui Gong,[1,2]* Boyang Liu,[2] Yizhou Zhu,[2] Shaomao Xu,[1,2] Yonggang Yao,[2] Wei Luo,[2] Chengwei Wang,[1,2] Steven D. Lacey,[2] Jiaqi Dai,[2] Yanan Chen,[2] Yifei Mo,[1,2] Eric Wachsman,[1,2]† Liangbing Hu[1,2]†

Solid-state batteries are a promising option toward high energy and power densities due to the use of lithium (Li) metal as an anode. Among all solid electrolyte materials ranging from sulfides to oxides and oxynitrides, cubic garnet–type $Li_7La_3Zr_2O_{12}$ (LLZO) ceramic electrolytes are superior candidates because of their high ionic conductivity (10^{-3} to 10^{-4} S/cm) and good stability against Li metal. However, garnet solid electrolytes generally have poor contact with Li metal, which causes high resistance and uneven current distribution at the interface. To address this challenge, we demonstrate a strategy to engineer the garnet solid electrolyte and the Li metal interface by forming an intermediary Li-metal alloy, which changes the wettability of the garnet surface (lithiophobic to lithiophilic) and reduces the interface resistance by more than an order of magnitude: 950 ohm·cm^2 for the pristine garnet/Li and 75 ohm·cm^2 for the surface-engineered garnet/Li. $Li_7La_{2.75}Ca_{0.25}Zr_{1.75}Nb_{0.25}O_{12}$ (LLCZN) was selected as the solid-state electrolyte (SSE) in this work because of its low sintering temperature, stabilized cubic garnet phase, and high ionic conductivity. This low area-specific resistance enables a solid-state garnet SSE/Li metal configuration and promotes the development of a hybrid electrolyte system. The hybrid system uses the improved solid-state garnet SSE Li metal anode and a thin liquid electrolyte cathode interfacial layer. This work provides new ways to address the garnet SSE wetting issue against Li and get more stable cell performances based on the hybrid electrolyte system for Li-ion, Li-sulfur, and Li-oxygen batteries toward the next generation of Li metal batteries.

INTRODUCTION

Lithium (Li) metal anodes are important in developing both high-energy and power density batteries with Li-containing cathodes or non–Li-containing cathodes (sulfur and air/O_2) (1, 2). Li metal has the highest theoretical capacity (3860 mAh/g) and the lowest electrochemical potential (−3.04 V versus the standard hydrogen electrode) and is, thus, the preferred anode material among Li battery chemistries (3, 4). In liquid electrolyte systems, Li dendrites have been the main challenge for decades (5, 6). Li dendrite formation and propagation in liquid electrolytes pose major safety and electrochemical performance concerns, which hamper long-term battery cycling (3). Attempts have been made to reduce and mitigate Li dendrites in liquid electrolyte systems through the use of separators (7–10), electrolyte additives (11–13), and Li-hosted matrices (14–17). An effective strategy to address this fundamental challenge remains elusive, and investigations are ongoing. In addition, the intrinsic properties of organic liquid electrolytes such as high toxicity, narrow chemical stability window, and low thermal stability are inevitable hazards that affect their broad application.

Solid-state batteries (SSBs) permit Li metal anodes because the solid nature of the electrolyte can effectively block Li dendrites and provide a large electrochemical stability window (0 to 5 V), superior thermal stability, and direct multiple cell stacking for high-voltage designs (18–21). This nonliquid system allows batteries to tolerate both high voltages and temperatures, which enable SSBs to be safer and have higher energy densities than liquid electrolyte systems. SSB performance relies on the properties of the solid-state electrolyte (SSE) (22). Among the solid electrolyte materials that range from sulfides to oxides and oxynitrides, most have a relatively low ionic conductivity or deliver an unstable interface against Li metal (23–29). Sulfide-type materials, such as $Li_{10}GeP_2S_{12}$ (LGPS), have a high ionic conductivity (10^{-2} S/cm) but are highly sensitive to moisture and are limited due to Li interface instabilities. Oxide-type materials, such as $Li_xLa_{2/3-x}TiO_3$ (LLTO), have a high ionic conductivity (10^{-3} S/cm) but are not stable against Li as well. Oxynitride-type materials, such as $Li_{3.3}PO_{3.9}N_{0.17}$ (LiPON), have a good stability with Li metal but have a low ionic conductivity (10^{-6} S/cm) (30). In addition, the solid electrolyte synthesis method and battery fabrication procedures are other important considerations for SSBs. Therefore, a good SSE should include the following characteristics: high ionic conductivity, wide electrochemical stability window, good chemical stability with Li metal anodes, inexpensive, and the ability to facilitate a facile fabrication process.

Recently, first-principle calculations indicate that almost all SSE materials are thermodynamically unstable against Li; however, among all of the SSEs, garnet-type SSEs exhibit the lowest reduction potential against Li and present the most thermodynamically stable interface with Li. Therefore, garnet SSE materials are the most favorable to use with Li metal anodes (27). On the basis of the calculation results and experimental performance, garnet-type $Li_7La_3Zr_2O_{12}$ (LLZO) is the most-promising material for SSE/Li metal SSBs due to LLZO's high ionic conductivity (10^{-3} to 10^{-4} S/cm) and good stability against Li (26, 31).

Although garnet-type materials exhibit promising chemical and electrochemical stability with Li metal, there is poor interfacial wetting between Li metal and oxide ceramics, which prevents intimate physical contact (32–34). Poor physical contact would lead to high interfacial resistance in the range of 10^2 to 10^3 ohm·cm^2 and inhomogeneous current distribution. As a result, the cell polarization becomes large

[1]University of Maryland Energy Research Center, University of Maryland, College Park, MD 20742, USA. [2]Department of Materials Science and Engineering, University of Maryland, College Park, MD 20742, USA.
*These authors contributed equally to this work.
†Corresponding author. Email: binghu@umd.edu (L.H.); ewach@umd.edu (E.W.)

and intensifies with increased cycle time and current density. Attempts have been made to decrease the interface resistance by applying high external pressure to improve the physical contact, removing the Li_2CO_3 passivation layer, and controlling the garnet's microstructure and grain boundary sizes (35). To the best of our knowledge, none of these efforts have sufficiently decreased the interface resistance. Therefore, one of the main obstacles for achieving successful solid-state Li batteries is minimizing the interfacial resistance between the SSE and the Li metal anode (18).

Here, we modify the garnet solid electrolyte and Li metal interface by forming an ultrathin, artificial intermediary Li-metal alloy layer to increase the Li wettability of the garnet surface. A low interfacial resistance of tens of ohm·cm^2 can be achieved, which approaches the current state-of-the-art Li-ion batteries (LIBs). In our design, a thin layer of Al is introduced to form an ionically conducting Li-Al alloy that acts as an interfacial layer between the garnet SSE and the Li metal anode. By forming a Li-Al alloy at the interface, the garnet surface becomes lithiophilic (Li metal wets the garnet surface), which provides good physical contact between the SSE and the Li metal and decreases the area-specific resistance (ASR), which is good for ion transport. In this way, the polarization is minimized, and the interfacial resistance is stabilized. Figure 1A schematically depicts the interface morphologies of the garnet electrolyte and Li anode. The pristine garnet SSE has poor contact with the Li metal and gaps remain at the interface; however, the Al coating will alloy with the Li metal and enable the garnet SSE to be fully coated with the Li metal. This engineered interface uses more of the garnet's surface area and facilitates even ion and electron transfer. With the Li-Al alloy

interface, the interfacial resistance was reduced from 950 to 75 ohm·cm^2 at room temperature (20°C). We also investigated the interfacial resistance as a function of temperature, and the results indicate that the interfacial resistance was greatly reduced at elevated temperatures. For example, the interfacial resistance was reduced to 30 ohm·cm^2 at 60°C. Galvanostatic Li stripping and plating in symmetric cells exhibited a flat voltage plateau, illustrating a stable interfacial resistance as Li diffuses back and forth through the Li-Al alloy interface.

On the basis of the solid-state garnet SSE and Li metal configuration, we demonstrated a hybrid solid-liquid electrolyte system. The hybrid system uses the improved solid-state garnet SSE Li metal anode and a thin liquid electrolyte cathode interfacial layer. It is known that the hybrid solid-liquid electrolyte can suppress unwanted redox shuttles and will be a promising option for high-energy batteries (36). A general method is to introduce the liquid phase by using liquid electrolyte as an interfacial layer for both Li metal and cathodes. Extensive studies have been carried out to fundamentally understand the solid-liquid electrolyte interface and develop full cells based on hybrid solid-liquid electrolyte for Li metal batteries (37–44). To achieve Li metal battery with minimum liquid electrolyte, it is desirable to adopt our proposed hybrid electrolyte system that has solid-state garnet SSE/Li in the anode and uses a small amount of liquid electrolyte in the cathode to design advanced Li metal batteries. Therefore, this work provides new ways to address the garnet SSE wetting issue against Li and get more stable cell performances based on the advanced hybrid solid-liquid electrolyte system for Li-ion, Li-sulfur, and Li-oxygen batteries, paving the way for next-generation Li metal batteries (Fig. 1B).
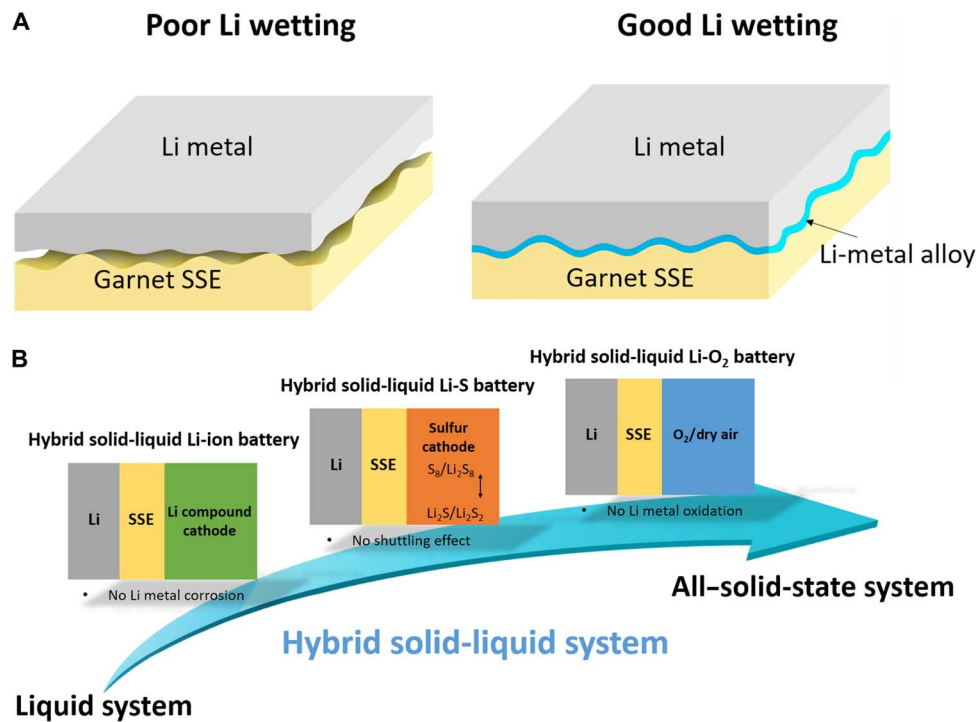
Fig. 1. Schematic of improved wettability of SSE against Li metal and demonstration of hybrid solid-liquid electrolyte system for Li-ion, Li-S, and Li-O$_2$ batteries. (**A**) Schematic of engineered garnet SSE/Li interface using Li-metal alloy. The pristine garnet SSE has poor contact with Li. Al-coated garnet SSE exhibits good contact with Li due to the Li-Al alloy that forms between the SSE and the Li metal. The garnet SSE surface becomes "lithiophilic," enabling a low ASR when Li metal is used. (**B**) Schematic of the hybrid solid-liquid electrolyte system for Li-ion, Li-S, and Li-O$_2$ batteries. Solid-state garnet SSE/Li is on the anode side, and liquid electrolyte is applied to the cathode side.

RESULTS
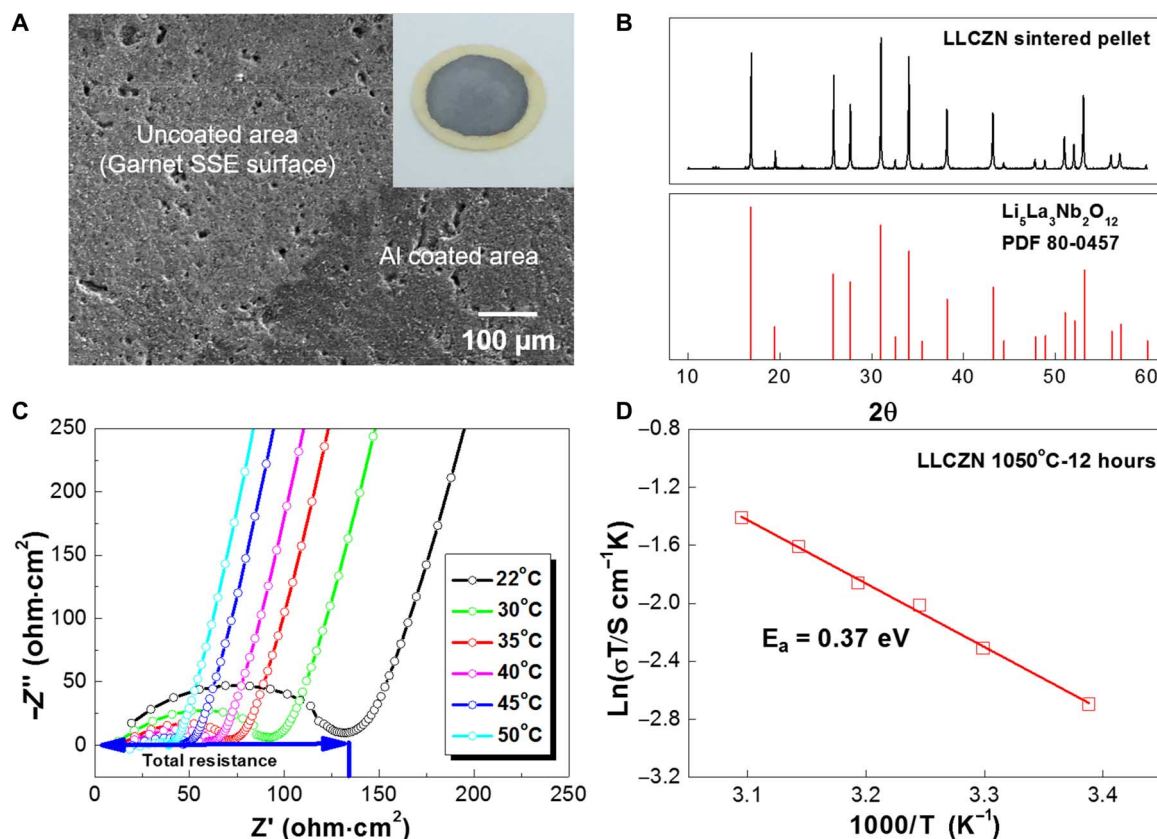
Characterization of garnet SSE

$Li_7La_{2.75}Ca_{0.25}Zr_{1.75}Nb_{0.25}O_{12}$ (LLCZN) was selected as the SSE in this work because of its low sintering temperature, stabilized cubic garnet phase, and high ionic conductivity (45). LLCZN was synthesized using a modified sol-gel method, followed by thermal sintering (see details in Materials and Methods). The density of the sintered pellet (92% of the theoretical value) was measured by the Archimedes method in ethanol. Figure 2A shows the polished surface structure of the sintered garnet (bright area) and Al coating (dark area). Some isolated pores remained in the sintered pellet surface after polishing. A cross section of the garnet ceramic disc exhibits the micrometer-sized garnet grains sintered together to form a solid electrolyte with a 20-nm-thick Al layer coating (fig. S1). The Al coating conformed to the polished garnet surface with the use of the vapor deposition method (figs. S2 and S3). The inset of Fig. 2A is a digital image of the Al-coated garnet ceramic disc with a gray Al coating on a yellow garnet ceramic. X-ray diffraction (XRD) was used to analyze the phase of the sintered LLCZN pellet in Fig. 2B. The peaks match well with cubic garnet $Li_5La_3Nb_2O_{12}$ (PDF 80-0457). $Li_5La_3M_2O_5$ (M = Nb, Ta) is the first structural example of a rapid, Li-ion conductive garnet and is the conventional structure used to study the garnet-type LLZO materials (26, 46–48). Electrochemical impedance spectroscopy (EIS) was used to measure the Li-ion conductivity of sintered LLCZN. The impedance curves measured from room temperature to 50°C were plotted in the Nyquist form, as shown in Fig. 2C. All the Nyquist plots are composed of a semicircle at medium frequency and a nearly vertical low-frequency tail. The real axis intercept at high frequency can be assigned to the LLCZN bulk resistance, whereas the depressed arc is associated with the grain boundary response. The total resistance of both the bulk and grain boundary contributions is calculated using the low-frequency intercept. The low-frequency tail corresponds to the capacitive behavior of the gold electrodes, which blocks Li-ion diffusion. Because Li-ion conduction in LLCZN is thermally activated, the total pellet resistance decreases as the temperature increases. The logarithmic conductivity is plotted against the inverse of temperature, and the activation energy of Li-ion conduction (0.37 eV) is calculated using the Arrhenius equation (Fig. 2D).
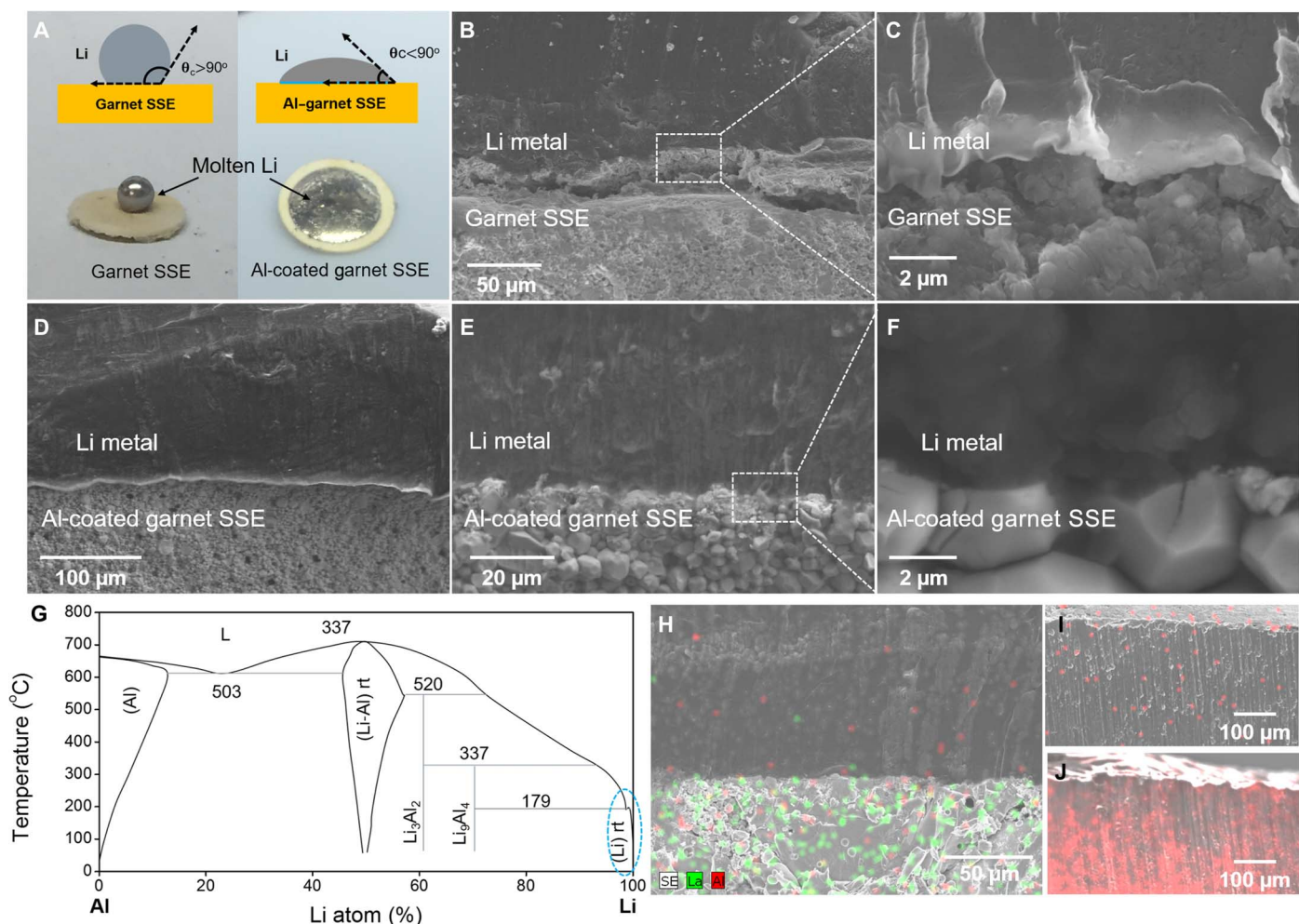
Li wetting behavior of SSE.

A droplet of molten Li was applied to the garnet and Al-coated garnet surfaces to observe the material's wettability. As shown in Fig. 3A, for the pure garnet, the molten Li instantly formed a ball on top of the garnet disc, which demonstrates poor wetting. For the Al-coated garnet, the molten Li spread out quickly, which covered the engineered garnet surface. Note that an obtuse contact angle indicates poor Li contact with the uncoated garnet due to Li's higher surface energy than the garnet; an acute angle demonstrates good wettability between Li and the Al coating on the garnet surface.

The interface morphology was characterized by SEM, as shown in Fig. 3 (B to F), which compares the Li wetting behavior of garnet SSE with/without an Al coating. Because of poor wetting with pristine garnet, only a small Li contact area can be used to characterize the interface morphology for the Li | garnet SSE sample. As shown in

Fig. 2. Characterization of LLCZN SSE. (**A**) Scanning electron microscopy (SEM) image of the surface morphology of the Al-coated LLCZN ceramic surface. The inset is a digital image of an Al-coated LLCZN ceramic disc. The yellow ceramic disc is coated by Al and appears gray in color. (**B**) XRD pattern of the as-synthesized LLCZN. (**C**) EIS profiles of the LLCZN at different temperatures. (**D**) Arrhenius plot of LLCZN conductivity.

Fig. 3. Wetting behavior and interfacial morphology characterization of Li | garnet SSE and Li | Al-coated garnet SSE. (**A**) Wetting behavior of molten Li with garnet SSE and Al-coated garnet SSE. The inset is a schematic showing the contact angles of a molten Li droplet wetting the surface of both uncoated and Al-coated garnet SSEs. Improved Li wettability is demonstrated after Al-coating the garnet surface. (**B** and **C**) SEM images of Li | garnet SSE, showing the poor Li wettability of uncoated garnet. (**D** to **F**) SEM images of Li | Al–garnet SSE–Al exhibiting superior Li wettability with Al-coated garnet. (**G**) Phase diagram of Li-Al. (**H**) Elemental mapping of Li | Al–garnet SSE in cross section. The Al signal was detected in bulk Li. (**I** and **J**) Elemental mapping of the very top area of Li metal to show the diffusion process of Al.

Fig. 3 (B and C), a large gap separated the top Li metal and the bottom garnet. Only a few contact spots can be observed, which illustrates that proper Li wetting is crucial to reduce the interfacial resistance of Li and the garnet (49). Elemental mapping of the Li | garnet SSE sample shows La and Al distribution on the cross section (fig. S4). Al in the garnet sample was from the contamination of Al_2O_3 crucible during sample preparation and sintering. Previous results show that small grains and multiple grain boundaries at the garnet interface can greatly reduce the interfacial resistance with Li (35). These small grains and multiple grain boundaries are directly related to interface roughness, which may increase the probability of the garnet contacting Li metal and reducing interfacial resistance. If the interfaces become rougher, then their total contact area will be increased, causing less interfacial resistance; however, the Li wettability with garnet remains an issue.

As seen in Fig. 3 (D to F), the Al-coated garnet maintains superior contact with Li, due to the formation of a Li-Al alloy at the interface. The magnified SEM image illustrates the intimate contact between the Li and garnet due to the conformal Al coating and Li-Al interfacial layer (Fig. 3F). Moreover, we can see that Li filled the pores of the garnet

particles and grain boundaries, which greatly increases the Li-garnet contact area. Al signal was detected in the bulk Li metal of the Li | Al-coated garnet SSE sample (Fig. 3H and fig. S5), indicating the diffusion of Al into the molten Li. When alloying with Li metal by heating, this ultrathin Al layer would be replaced by Li metal immediately and then migrate toward the bulk Li anode. Because the Li/Al weight ratio is near 100% (see the Li-Al phase diagram in Fig. 3G), the solid solution can be considered as a pure Li phase. An additional experiment was carried out to show the Al diffusion process. Al foils of two different thicknesses (5 and 30 μm thick) were placed underneath a 1-mm-thick Li metal foil to heat together at 200°C. We noticed that the Al foil completely corroded and dissolved into the molten Li. By examining the cross section of the Li metal, the Al signal can be detected on the very top part of the Li metal, showing different Li concentrations (Fig. 3, I and J). This observation can simulate the condition of the Al coating diffusing into the molten Li state on the garnet surface. It is anticipated that the ultrathin Al coating (20 nm) could have a fast diffusion into molten Li. To determine the Li-Al alloy phase, we used XRD to detect the lithiated Al coating on the garnet ceramic disc. The

pristine Al coating became dark in contact with molten Li. XRD identified the Li-Al and Li_3Al_2 peaks in the conformal coating layer (fig. S6), yet a Li_9Al_4 phase may mainly form on the interface based on the Li-Al phase diagram. We will carry out more work in the future to understand the composition of the alloy formation at the interface.

Electrochemical evaluation of interfacial resistance.

The interfacial resistance was evaluated by EIS for Li | garnet SSE | Li symmetric cells. The symmetric cells were prepared following the schematic shown in Fig. 4A. The SSE was sandwiched between two fresh Li metal foils and then covered by stainless steel plates to block Li diffusion. The cells were heated on a hot plate at 200°C in an argon-filled glove box to melt the Li. The digital image in Fig. 4A depicts the symmetric cell's structure, and the preparation process is shown in fig. S7. The size of the stainless steel plates was cut to match the Li and attached to the Li surface gently by hand. The stainless steel plates prevent oxidation of Li on the outer surface during heating. Note that no high external pressure was applied to the garnet and Li system. Two symmetric cells, Li | garnet SSE | Li and Li | Al–garnet SSE–Al | Li, were prepared and tested directly in an argon-filled glove box. The two cells showed significant differences in total resistance, which depend on both the garnet's total resistance and the interface charge transfer resistance, as shown in the Nyquist plots (Fig. 4, B and C). The Li | garnet SSE | Li cell had a total resistance of ~2000 ohm·cm²; however, the Li | Al–garnet SSE–Al | Li cell exhibited a resistance of ~300 ohm·cm², which is almost one order of magnitude smaller than the uncoated SSE. The small partial semicircle at high frequency can be assigned to the total resistance of the garnet material. The large semicircle at medium frequency and low frequency corresponds to the charge transfer resistance, which is the combination of the SSE resistance and the Li interfaces within the symmetric cells. The decreased size of the semicircle indicates that the interfacial resistance was significantly reduced using the Al coating. The total garnet resistance was ~150 ohm·cm² and remained unchanged during the Li melting process (49). By subtracting the garnet ASR, the Li | garnet SSE | Li cell charge transfer resistance was ~1900 ohm·cm² at 20°C. For the Li | Al–garnet SSE–Al | Li cell, the charge transfer resistance was decreased to ~150 ohm·cm². Note that the interfacial resistance corresponds to two symmetric interfaces. The interfacial resistance is ~950 and ~75 ohm·cm² for Li | garnet SSE and Li | Al–garnet SSE–Al, respectively.

The temperature-dependent interfacial resistance was characterized using EIS at temperatures from 30° to 80°C. In Fig. 4D, the total impedance of the Li | Al–garnet SSE–Al | Li cell decreased as the temperature increased. The semicircle at medium and low frequency decreased, which indicates that the Li-Al alloy interfacial resistance negatively correlated with temperature. The interfacial resistance was calculated by subtracting the total resistance of the garnet material, and the data were plotted as a function of temperature (Fig. 4E). The interfacial resistance reduced with temperature: ~75 ohm·cm² at 20°C, ~27 ohm·cm² at 60°C, and ~20 ohm·cm² at 80°C. These values are approaching the typical LIB impedance of tens of ohm·cm².

The interface stability was measured by galvanostatically charging and discharging at a constant current to plate/strip Li⁺ and mimicked the operation of Li metal batteries. Symmetric cells with two Li electrodes were prepared and assembled into 2032 coin cells (fig. S8). A highly conductive carbon sponge was used as a force absorber and placed on top of the symmetric cells to prevent the garnet ceramic disc from cracking during battery assembly. The cell was tightened using a battery clip, and epoxy resin was used to seal the coin cells (fig. S9). All the cells were assembled and tested in an argon-filled glove box at 20°C. Figure 4F shows the time-dependent voltage profile of the Li | garnet SSE | Li symmetric cell at a current density of 0.05 mA/cm². The positive and negative voltage denotes Li stripping and Li plating, respectively. The cell exhibited a high voltage (~0.2 V) for Li stripping and a low voltage (~0.1 V) for Li plating, which is likely due to contact area differences between garnet and Li, causing polarization to occur during stripping and plating. In each cycle, the voltage increased: The voltage of Li stripping in the first cycle increased from 0.12 to 0.16 V. With subsequent cycles, the voltage continuously increased, indicating an unstable interface where the interfacial resistance increases with time. Poor contact between Li and garnet is the likely culprit, causing large currents to accumulate at interfacial points/areas, which leads to substantial cell polarization. Therefore, a stable interface is important to decrease the polarization and maintain good cycling performance with SSE systems.

In contrast, the Al coating effectively stabilized the interfacial resistance during reversible Li stripping and plating. The symmetric Al-garnet-Al | Li cell was tested at 60°C at a current density of 0.05 mA/cm² for 24 hours, which delivered a capacity of 1.2 mAh (Fig. 4G). The mass of the stripped/plated Li, calculated using the theoretical capacity of Li metal (3860 mAh/g), was 0.31 mg, which accounts ~3.1% of the total ~10-mg Li metal used. We can see that the voltage shows a flat plateau, indicating stable Li-ion flow through the interface between garnet SSE and Li metal. The Li | Al–garnet SSE–Al | Li symmetric cell exhibited superior stability at a current density of 0.1 mA/cm² (Fig. 4, H and I). The symmetric cell was periodically cycled for 5 min. The cell exhibited a flat voltage of ±28 mV for each cycle, and the total resistance calculated using Ohm's law was ~280 ohm·cm², which is in good agreement with the EIS measurements. The bulk resistance of the garnet solid electrolyte was ~150 ohm·cm², which contributed 15 mV to the total voltage of the symmetric cell at this current density. When a higher current density of 0.2 mA/cm² was applied to the symmetric cell, the voltage increased to 75 mV with a calculated ASR of ~375 ohm·cm². The voltage plateau still remained flat, indicating a good interface between Li | Al–garnet SSE–Al (Fig. 4, J and K). Long-term cycling for over 30 hours was tested at a current density of 0.1 mA/cm². The overall voltage was smaller than 30 mV without major voltage fluctuations. When the current density doubled, the long-term cycling performance remained stable, and no voltage hysteresis was observed. After cycling, the cell was opened, and the cross section SEM images indicated that no morphological changes occurred at the interface due to cycling (fig. S10). The stable and constant stripping and plating voltages confirm that alloy formation is a promising strategy to address the fundamental wetting challenge of garnet SSEs with Li metal.

The conformal Al coating on the garnet ceramic disc drastically altered the garnet surface's Li wettability due to the formation of a Li-Al alloy. The reaction between Al and Li promotes enhanced molten Li infusion onto the garnet's rough surface, whereas the formation of a Li-Al alloy fills the gap between the garnet solid electrolyte and the Li metal to improve interfacial contact and enhance Li⁺ transport (50). In this case, a new interface between the Li metal anode and the garnet is formed (Fig. 5A). We applied first-principles calculations to investigate the interface stability between the garnet SSE and the intermediary Li-Al alloy layer using the approach defined in a previous work (28). By considering the interface as a pseudobinary system consisting of Li-Al alloy and garnet SSE, we identified the most thermodynamically favorable interface and calculated the mutual reaction
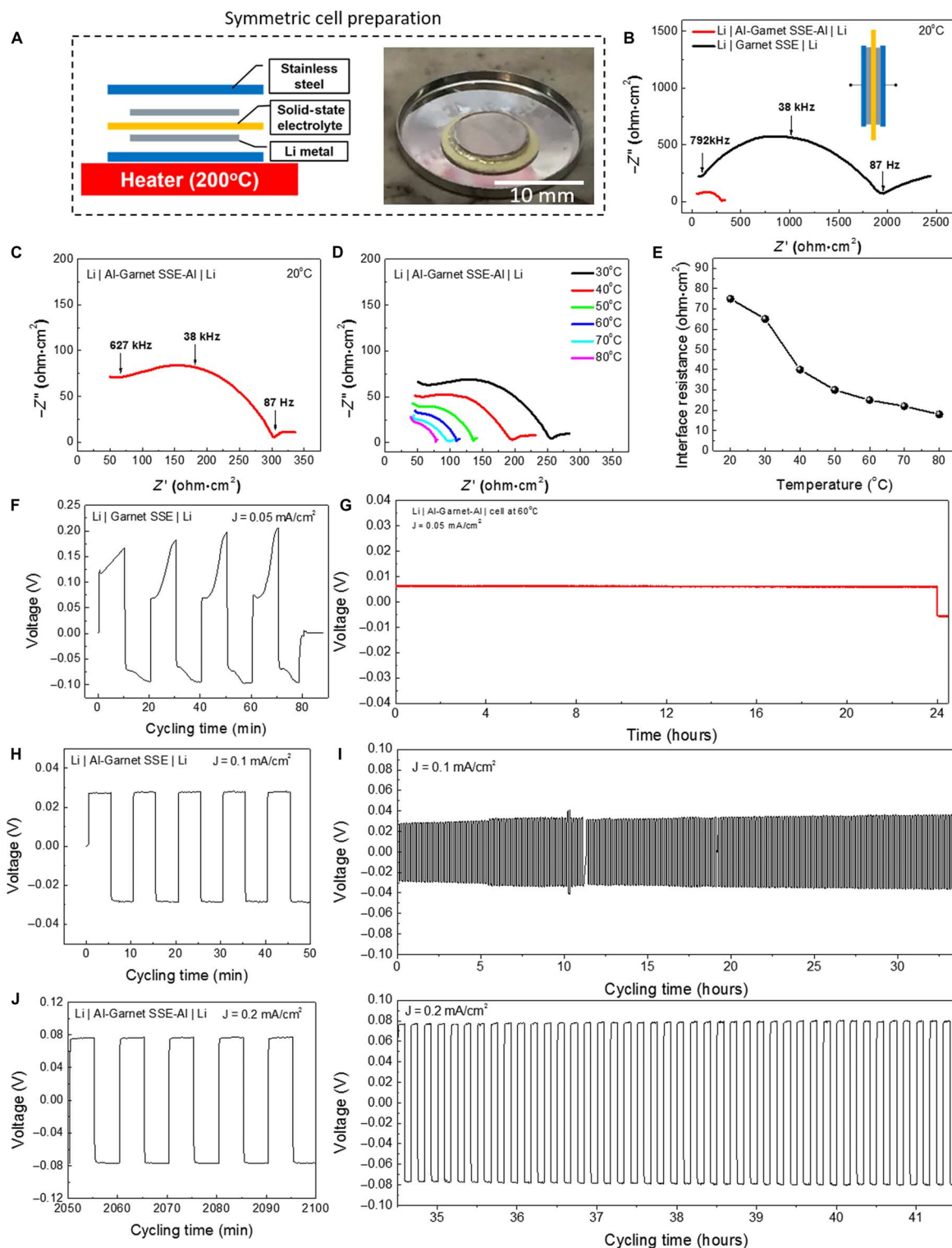
Fig. 4. Electrochemical stability of the Li and garnet interface. (**A**) Schematic of the symmetric cell preparation and a digital image of Li metal melting on a garnet SSE. (**B** and **C**) Comparison of Nyquist plots of Li | garnet SSE | Li and Li | Al–garnet SSE–Al | Li in the frequency of 1 MHz to 100 mHz at 20°C. (**D**) Nyquist plots of Li | Al–garnet SSE–Al | Li symmetric cell at various elevated temperatures. (**E**) The interfacial resistance of the Li | Al–garnet SSE–Al | Li symmetric cell as a function of temperature during heating. (**F**) Voltage profile depicting the Li plating/striping behavior for the Li | garnet SSE | Li symmetric cell at a current density of 0.05 mA/cm². The voltage plateau continued to increase each cycle due to the high polarization at the unfavorable Li/SSE interface. The high voltage range reflects the large interfacial resistance for the pristine garnet with Li metal. (**G**) Li plating of the symmetric Li | Al-garnet-Al | cell at 60°C with a current density of 0.05 mA/cm² for 24 hours. (**H** to **K**) Voltage profiles for the Li | Al–garnet SSE–Al | Li symmetric cell at current densities of 0.1 and 0.2 mA/cm². The voltage plateau remained flat and stable during cycling, which proves that the Li-Al alloy creates a stable interface between the garnet SSE and the Li metal. The low voltage range illustrates the small interfacial resistance in the cell.

energy between the two materials (28). The first-principles computation shows that Li-Al alloys and garnet SSE have stability with mutual reaction energies in the range of −60 to −40 meV/atom (Fig. 5B and table S1). This small amount of interfacial reaction indicates potential kinetic stabilization and the absence of significant interfacial degradation, as observed in other solid electrolytes (27, 28). In addition, these minor reactions significantly improve the wettability at the interface. Therefore, the interface between the Li-Al alloy and the garnet SSE may exhibit both good wettability and chemical stability, which enhance interfacial contacts and reduce interfacial resistance.

Performance of hybrid solid-liquid full cells

To demonstrate the hybrid solid-liquid system, we evaluated and prepared three types of cathodes (a Li-containing cathode compound, sulfur, and oxygen). The electrochemical performance of the hybrid solid-state LIBs using a Li iron phosphate ($LiFePO_4$) cathode is shown in Fig. 6 (A to C). Details of the full cell preparation and assembly are given in Materials and Methods. All the cells were tested at 20°C. The impedance profiles of the fresh and cycled hybrid solid-state LIBs are shown in Fig. 6A. The partial semicircle at high frequency is similar to the impedance profile of the symmetric Li | Al–garnet SSE–Al | Li cell. The large semicircle in the medium frequency is attributed to a mix of the charge transfer and diffusion processes in the liquid electrolyte system of the cathode. The fresh cell had an overall impedance of 1360 ohm·cm². After 100 cycles, the overall impedance decreased to 1260 ohm·cm². The slight decrease of the partial semicircle at high frequency demonstrates the reduced interfacial resistance of garnet SSE against Li metal after cycling. The charge and discharge profiles of the hybrid solid-state LIB cell are shown in Fig. 6B. The cathode active material has a loading of ~1.0 mg/cm². At a current density of 0.1 mA/cm², the cell delivered an initial charge and discharge capacity of 153 and 132 mAh/g, with 86% coulombic efficiency (defined as the ratio of charge capacity over discharge capacity). With further cycling, the capacities remain relatively stable (>120 mAh/g over 100 cycles). As shown in Fig. 6C, the coulombic efficiency was ~100%, and the cell exhibited good rate capability when higher current densities (0.2 and 0.3 mA/cm²) were applied.

Li-S and Li-O_2 chemistries were also demonstrated as hybrid solid-liquid electrolyte systems. Conventional Li-S batteries using liquid electrolyte suffer from the polysulfide shuttling effect and side reactions with Li metal that cause significant capacity decay and low coulombic efficiency. The hybrid SSE system can avoid these issues. The dense garnet SSE can physically block the dissolved polysulfides from reacting with the Li metal and locally confine the sulfur/polysulfide active materials to the cathode side. To demonstrate the garnet SSE blocking effect in the Li-S system, we used an elemental sulfur cathode to construct the hybrid solid-liquid Li-S battery full cell. A conventional liquid electrolyte, 1 M LiTFSI in DME/DOL [1:1 (v/v)], was applied to the sulfur cathode. The sulfur loading was ~1.0 mg/cm². The galvanostatic discharge and charge curves are shown in Fig. 6D. The initial discharge and charge capacities were 1532 and 1388 mAh/g, respectively, which correspond to 90.6% coulombic efficiency. The cycling performance exhibited both high capacity and >99% coulombic efficiency, which indicates that the garnet SSE can effectively block the polysulfide migration/shuttling effect for Li-S batteries (fig. S11). Note that the shuttling effect in liquid electrolyte–based Li-S batteries exhibits a higher charge capacity than the discharge capacity. In this system, the coulombic efficiency is typically defined as the ratio of discharge capacity over charge capacity. The cell performance degradation is possible due to the deposition of the dissolved sulfur and polysulfide materials into the isolated pores on garnet SSE surface (fig. S12). These deposited active materials lack sufficient electron transfer pathway and became "dead active materials" that cannot be used anymore, which leads to fast capacity decay. Garnet SSE remained stable, and no phase change after cycling in batteries was observed (fig. S13).

Similar to the shuttling effect in Li-S batteries, conventional Li-O_2 batteries suffer from the diffusion of oxygen through the electrolyte layer to Li metal, which forms an insulating oxide layer on the anode surface and increases interfacial resistance. In addition, to lower the charge overpotential, redox mediators are often used in the liquid electrolyte, which can directly react with the Li metal anode and induce unfavorable side reactions. By introducing this hybrid solid-liquid electrolyte, these challenges can be avoided because Li metal will not be oxidized by gaseous oxygen or corroded by redox mediators. Here, we demonstrate a hybrid solid-liquid Li-O_2 cell using a carbon cathode. Figure 6E displays the cell's electrochemical performance at a current density of 15 μA/cm² with a charge/discharge time limit of 10 hours. The cell can be cycled over 10 cycles and showed a stable flat discharge plateau at ~2.5 V.

Recently, an interface-engineered all–solid-state battery was developed to adopt a porous garnet electrolyte structure to enhance Li-ion
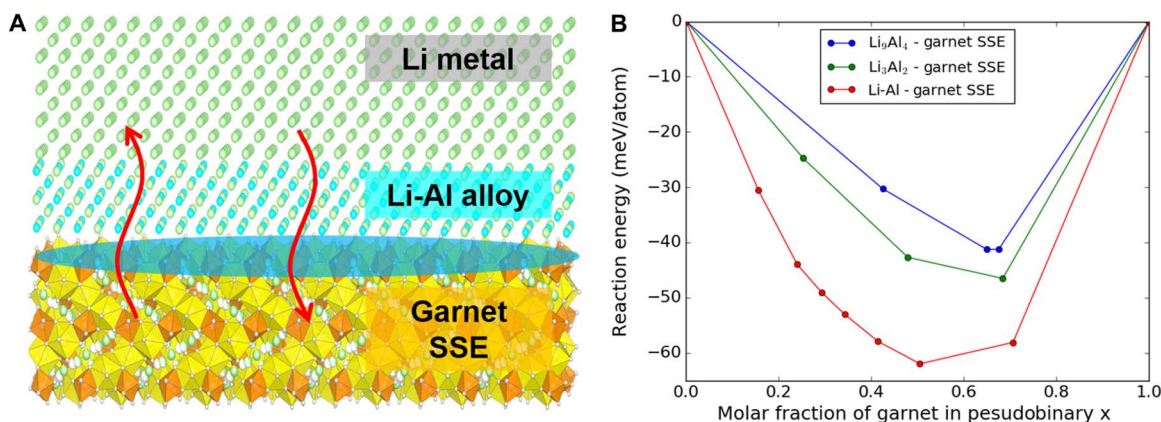
Fig. 5. Schematic and first-principles computation of the Li-Al alloy interface between the Li metal and the garnet SSE. (**A**) The reaction between Al and Li promotes enhanced molten Li infusion onto the garnet's rough surface, whereas the formation of a Li-Al alloy fills the gap between the garnet solid electrolyte and the Li metal to improve interfacial contact and enhance Li⁺ transport. (**B**) Calculated mutual reaction energy $\Delta E_{D,mutual}$ of the garnet and Li-Al alloy interfaces.
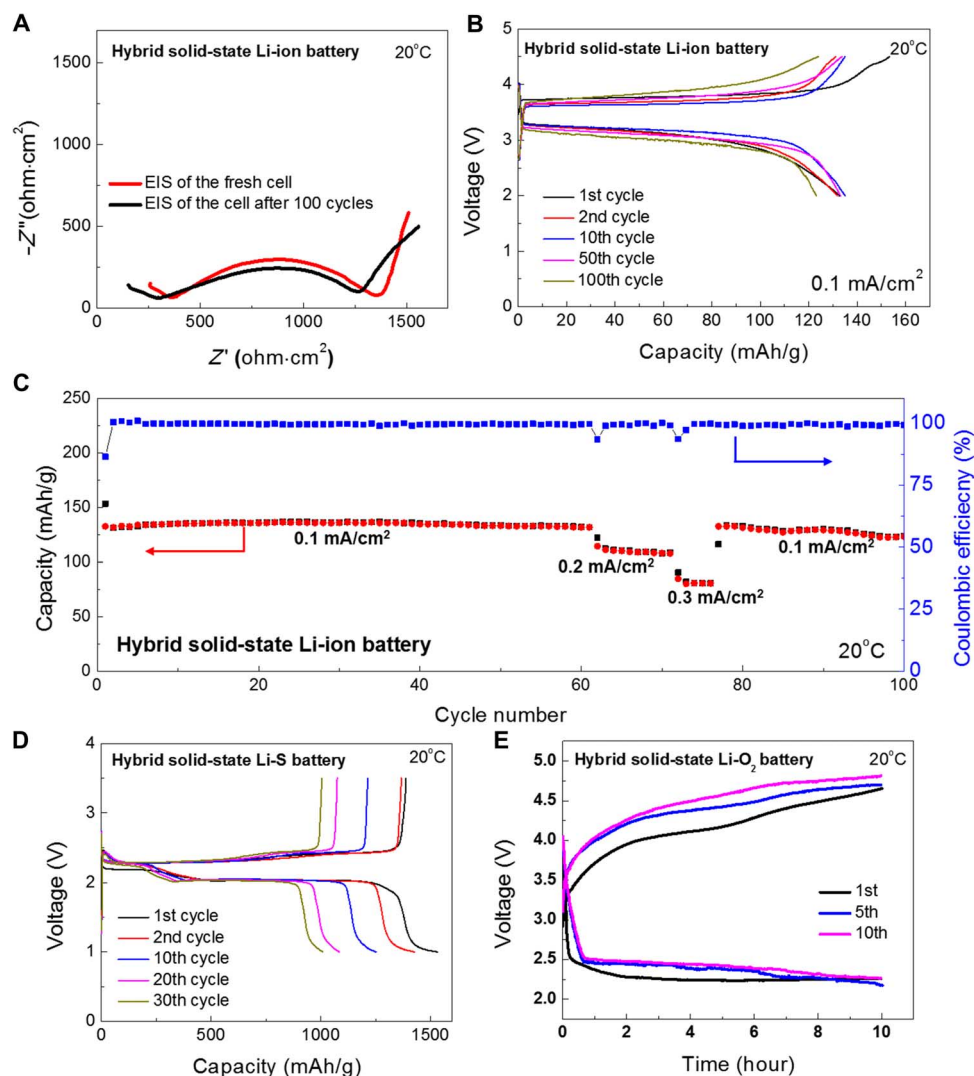
Fig. 6. Hybrid solid-state battery demonstrations. (**A**) EIS of the hybrid solid-liquid LIBs. LiFePO$_4$ cathode is used with a conventional electrolyte on the cathode side: 1 M LiPF$_6$ in ethylene carbonate (EC)/diethyl carbonate (DEC) [1:1 (v/v)]. (**B**) Galvanostatic charge/discharge profiles of the hybrid solid-liquid Li-ion cell. (**C**) Cycling performance of the cell over 100 cycles at different current densities. (**D**) Electrochemical performance of the hybrid solid-liquid Li-S cell. Elemental sulfur was used as the cathode, and 1 M LiTFSI in dimethoxyethane (DME)/1,3-dioxolane (DOL) [1:1 (v/v)] was used as the electrolyte on the cathode side. (**E**) Electrochemical performance of the hybrid solid-liquid Li-O$_2$ battery. Highly conductive carbon was used as the cathode, and 1 M LiTFSI in tetraethylene glycol dimethyl ether (TEGDME) was used on the cathode side.

transfer at the electrode-electrolyte interface with improved capacities and cycling performance (*51*). We envision that garnet structure with interface engineering can be designed into interconnected ion and electron networks for Li-S and Li-O$_2$ batteries to host dissolved sulfur/polysulfides or active catalysts with high surface areas. In addition, the porous garnet structure can be an ideal three-dimensional ion-conducting scaffold to confine Li in the cell during repeated cycling.

DISCUSSION

We demonstrate an effective strategy to modify the garnet solid electrolyte (LLCZN) and Li metal by introduction of an ultrathin conformal metal coating. We discovered that the metal layer would be immediately replaced by molten Li metal and then migrated toward the bulk Li metal. The alloying process significantly improves the wettability between the molten Li metal and the garnet SSE. By forming this Li-rich

solid solution, the garnet surface becomes lithiophilic, which allows the bulk Li electrode to conformally adhere to the garnet surface after solidification of molten Li metal. Because the Li/metal weight ratio is near 100%, their solid solution can be considered as a pure Li phase. As a result, intimate contact between garnet and Li metal is achieved, which decreases the interfacial resistance, minimizes polarization, and stabilizes the voltage plateau during Li stripping/plating. The interfacial resistance at 20°C was drastically reduced from 950 to 75 ohm·cm^2 using the Al-coated garnet SSE. The Li stripping and plating behavior of the symmetric cells exhibited a flat voltage plateau, demonstrating a stable charge transfer at the Li/garnet SSE interface. It is anticipated that a series of metals, which could be alloyed with molten Li, can be used to modify the interface wettability with Li metal. In current stage, this work has addressed the main challenge of surface wettability between a garnet SSE and an Li metal. In the future, we will focus on creating an artificial solid electrolyte interface layer to further stabilize the garnet SSE

interface in between a garnet SSE and a metallic Li anode. The advantages of the solid-state garnet SSE/Li metal configuration enable the development of a hybrid electrolyte system using the improved solid-state garnet SSE Li metal anode and a thin liquid electrolyte cathode interfacial layer. The hybrid electrolyte system exhibits good cell performances for different battery chemistries including Li-ion, Li-sulfur, and Li-oxygen batteries. This hybrid electrolyte design potentially avoids some fundamental challenges linked with conventional liquid-based electrolytes, such as Li dendrite growth, which paves the way for next-generation Li metal batteries.

MATERIALS AND METHODS

Garnet SSE preparation

The LLCZN powder was synthesized via a modified sol-gel method. The starting materials were $LiNO_3$ (99%, Alfa Aesar), $La(NO_3)_3$ (99.9%, Alfa Aesar), $Ca(NO_3)_2$ (99.9%, Sigma-Aldrich), $ZrO(NO_3)_2$ (99.9%, Alfa Asear), and $NbCl_5$ (99.99%, Alfa Aesar). Stoichiometric amounts of these chemicals were dissolved in deionized water, and 10% excess $LiNO_3$ was added to compensate for Li volatilization during the high-temperature pellet preparation. Citric acid and ethylene glycol (1:1 mole ratio) were added to the solution. The solution was evaporated at 120°C for 12 hours to produce the precursor gel and then calcined to 400° and 800°C for 5 hours to synthesize the garnet powder. The garnet powders were then uniaxially pressed into pellets and sintered at 1050°C for 12 hours covered by the same type of powder. The sintered LLCZN pellets were polished to a thickness of ~300 μm with a smooth surface. For the Al coating, 20 nm of Al was deposited using an Angstrom NexDep Ebeam evaporator at a rate of 0.2 nm/s. The pressure was kept below 5×10^{-6} torr during the deposition process.

Material characterization

The phase analysis was performed with powder XRD on a D8 Advance with LynxEye and SolX (Bruker AXS) using a Cu Kα radiation source operated at 40 kV and 40 mA. The morphology of the samples was examined by a field emission SEM (JEOL 2100F).

Electrochemical characterization

The symmetric Li | SSE | Li cell was prepared and assembled in an argon-filled glove box. The garnet electrolyte ceramic disc was wet-polished using sandpaper (400 and 800 grit) and rinsed with isopropanol alcohol several times. The thickness (300 μm) of the garnet ceramic was controlled. To measure the ionic conductivity of the garnet SSE, we coated a Au paste on both sides of the ceramic disc, and it acted as a blocking electrode. The gold electrodes were sintered at 700°C to form good contact with the ceramic pellet. To prepare the nonblocking cell with Li metal, we pressed Li granular (99%, Sigma) into fresh Li foil, and then we polished the surface to remove the oxidized layer. Fresh Li electrodes were then attached to the ceramic disc's surfaces and gently pressed by hand. The symmetric cell was placed in between the stainless steel plates and heated at 170°C to soften the Li metal before being gently pressed by hand to improve contact with the stainless steel. The symmetric cell was heated to 200°C to melt the Li and naturally cooled down to room temperature. The symmetric cell was then assembled into a 2032 coin cell with a highly conductive carbon sponge. The carbon sponge acted as the force absorber and prevented the garnet ceramic disc from being damaged. Battery test clips were used to hold and provide good contact with the coin cell. The edge of the cell was sealed with an epoxy resin. The EIS was performed in a frequency range of 1 MHz to 100 mHz with a 50-mV perturbation amplitude. Conductivities were calculated using $\sigma = L/(Z \times A)$, where Z is the impedance for the real axis in the Nyquist plot, L is the garnet ceramic disc length, and A is the surface area. The activation energies were obtained from the conductivities as a function of temperature using the Arrhenius equation. The symmetric cell was tested on a homemade hotplate. The galvanostatic Li stripping and plating test was performed with a Bio-Logic MPG-2 battery cycler. All the cells were tested in an argon-filled glove box.

First-principles computation

We considered the interface as a pseudobinary of Li-Al alloy and garnet SSE using the same approach as defined in previous work (28, 52). The phase diagrams were constructed to identify possible thermodynamically favorable reactions. The energies for the materials used in our study were obtained from the Materials Project database (53), and the compositional phase diagrams were constructed using the pymatgen package (54). The mutual reaction energy of the pseudobinary is calculated using the same approach as defined in our previous work (28).

Hybrid solid-state battery preparation and evaluation

All the cells were assembled in an argon-filled glove box. The hybrid solid-state cells were assembled in 2032 coin cells following the similar schematic shown in fig. S8. The electrode slurry coating method was carried out in ambient environment. The $LiFePO_4$ electrode consisted of 70% commercial $LiFePO_4$ powder (MTI Corporation), 20% carbon black, and 10% polyvinylidene fluoride (PVDF) binder in N-methyl-2-pyrrolidone (NMP) solvent. The electrode was dried in vacuum at 100°C for 24 hours. $LiPF_6$ (1 M) in a mixture of EC and DEC [1:1 (v/v)] was used as the electrolyte for the hybrid solid-state LIBs. The galvanostatic charge and discharge test was measured using a cutoff voltage window of 2 to 4.5 V. The sulfur electrode consists of 70% elemental sulfur powder (Sigma), 20% carbon black, and 10% polyvinylpyrrolidone (Sigma, $M_w = 360,000$) binder in water. The electrode was dried in vacuum at 60°C for 24 hours. Bis(trifluoromethane)sulfonimide Li salt (1 M) (LiTFSI, Sigma) in a mixture of DME and DOL [1:1 (v/v)] was used as the electrolyte for the hybrid solid-state Li-S batteries. The galvanostatic discharge and charge test was measured using a cutoff voltage window of 1 to 3.5 V. The carbon cathode for the Li-O_2 battery consists of 90% high-conductivity carbon (Ketjen Black EC600JD) and 10% PVDF binder in an NMP solvent. The slurry was casted onto a gas diffusion layer (Toray carbon paper) and dried under vacuum at 100°C for 24 hours. LiTFSI (1 M) in TEGDME acted as the electrolyte for the hybrid solid-state Li-O_2 batteries. The battery was tested under a current density of 15 μA/cm^2 with a charge/discharge time limit of 10 hours.

SUPPLEMENTARY MATERIALS

fig. S12. SEM image of the garnet SSE in cycled Li-S cell.
fig. S13. XRD profile of the garnet after cycling in Li-S cell.
table S1. The phase equilibria and decomposition energies of the garnet SSE and Li-Al alloy interfaces.

REFERENCES AND NOTES

1. M. Armand, J.-M. Tarascon, Building better batteries. *Nature* **451**, 652–657 (2008).
2. B. Scrosati, J. Garche, Lithium batteries: Status, prospects and future. *J. Power Sources* **195**, 2419–2430 (2010).
3. W. Xu, J. Wang, F. Ding, X. Chen, E. Nasybulin, Y. Zhang, J.-G. Zhang, Lithium metal anodes for rechargeable batteries. *Energy Environ. Sci.* **7**, 513–537 (2014).
4. H. Kim, G. Jeong, Y.-U. Kim, J.-H. Kim, C.-M. Park, H.-J. Sohn, Metallic anodes for next generation secondary batteries. *Chem. Soc. Rev.* **42**, 9011–9034 (2013).
5. C. Brissot, M. Rosso, J.-N. Chazalviel, S. Lascaud, Dendritic growth mechanisms in lithium/polymer cells. *J. Power Sources* **81–82**, 925–929 (1999).
6. D. Aurbach, E. Zinigrad, Y. Cohen, H. Teller, A short review of failure mechanisms of lithium metal and lithiated graphite anodes in liquid electrolyte solutions. *Solid State Ion.* **148**, 405–416 (2002).
7. S.-O. Tung, S. Ho, M. Yang, R. Zhang, N. A. Kotov, A dendrite-suppressing composite ion conductor from aramid nanofibres. *Nat. Commun.* **6**, 6152 (2015).
8. M.-H. Ryou, D. Jin Lee, J.-N. Lee, Y. Min Lee, J.-K. Park, J. Wook Choi, Excellent cycle life of lithium-metal anodes in lithium-ion batteries with mussel-inspired polydopamine-coated separators. *Adv. Energy Mater.* **2**, 645–650 (2012).
9. H. Wu, D. Zhuo, D. Kong, Y. Cui, Improving battery safety by early detection of internal shorting with a bifunctional separator. *Nat. Commun.* **5**, 5193 (2014).
10. W. Luo, L. Zhou, K. Fu, Z. Yang, J. Wan, M. Manno, Y. Yao, H. Zhu, B. Yang, L. Hu, A thermally conductive separator for stable Li metal anodes. *Nano Lett.* **15**, 6149–6154 (2015).
11. J. Qian, W. A. Henderson, W. Xu, P. Bhattacharya, M. Engelhard, O. Borodin, J.-G. Zhang, High rate and stable cycling of lithium metal anode. *Nat. Commun.* **6**, 6362 (2015).
12. Y. Lu, Z. Tu, L. A. Archer, Stable lithium electrodeposition in liquid and nanoporous solid electrlytes. *Nat. Mater.* **13**, 961–969 (2014).
13. N.-W. Li, Y.-X. Yin, C.-P. Yang, Y.-G. Guo, An artificial solid electrolyte interphase layer for stable lithium metal anodes. *Adv. Mater.* **28**, 1853–1858 (2016).
14. Z. Liang, D. Lin, J. Zhao, Z. Lu, Y. Liu, C. Liu, Y. Lu, H. Wang, K. Yan, X. Tao, Y. Cui, Composite lithium metal anode by melt infusion of lithium into a 3D conducting scaffold with lithiophilic coating. *Proc. Natl. Acad. Sci. U.S.A.* **113**, 2862–2867 (2016).
15. D. Lin, Y. Liu, Z. Liang, H.-W. Lee, J. Sun, H. Wang, K. Yan, J. Xie, Y. Cui, Layered reduced graphene oxide with nanoscale interlayer gaps as a stable host for lithium metal anodes. *Nat. Nanotechnol.* **11**, 626–632 (2016).
16. Y. Liu, D. Lin, Z. Liang, J. Zhao, K. Yan, Y. Cui, Lithium-coated polymeric matrix as a minimum volume-change and dendrite-free lithium metal anode. *Nat. Commun.* **7**, 10992 (2016).
17. C.-P. Yang, Y.-X. Yin, S.-F. Zhang, N.-W. Li, Y.-G. Guo, Accommodating lithium into 3D current collectors with a submicron skeleton towards long-life lithium metal anodes. *Nat. Commun.* **6**, 8058 (2015).
18. A. C. Luntz, J. Voss, K. Reuter, Interfacial challenges in solid-state Li ion batteries. *J. Phys. Chem. Lett.* **6**, 4599–4604 (2015).
19. J. Li, C. Ma, M. Chi, C. Liang, N. J. Dudney, Solid electrolyte: The key for high-voltage lithium batteries. *Adv. Energy Mater.* **5**, 1401408 (2015).
20. Y. Wang, W. Davidson Richards, S. P. Ong, L. J. Miara, J. Chul Kim, Y. Mo, G. Ceder, Design principles for solid-state lithium superionic conductors. *Nat. Mater.* **14**, 1026–1031 (2015).
21. K. K. Fu, Y. Gong, J. Dai, A. Gong, X. Han, Y. Yao, C. Wang, Y. Wang, Y. Chen, C. Yan, Y. Li, E. D. Wachsman, L. Hu, Flexible, solid-state, ion-conducting membrane with 3D garnet nanofiber networks for lithium batteries. *Proc. Natl. Acad. Sci. U.S.A.* **13**, 7094–7099 (2016).
22. Y. Kato, S. Hori, T. Saito, K. Suzuki, M. Hirayama, A. Mitsui, M. Yonemura, H. Iba, R. Kanno, High-power all-solid-state batteries using sulfide superionic conductors. *Nat. Energy* **1**, 16030 (2016).
23. W. D. Richards, L. J. Miara, Y. Wang, J. C. Kim, G. Ceder, Interface stability in solid-state batteries. *Chem. Mater.* **28**, 266–273 (2016).
24. J. F. M. Oudenhoven, L. Baggetto, P. H. L. Notten, All-solid-state lithium-ion microbatteries: A review of various three-dimensional concepts. *Adv. Energy Mater.* **1**, 10–33 (2011).
25. J. G. Kim, B. Son, S. Mukherjee, N. Schuppert, A. Bates, O. Kwon, M. J. Choi, H. Y. Chung, S. Park, A review of lithium and non-lithium based solid state batteries. *J. Power Sources* **282**, 299–322 (2015).
26. V. Thangadurai, S. Narayanan, D. Pinzaru, Garnet-type solid-state fast Li ion conductors for Li batteries: Critical review. *Chem. Soc. Rev.* **43**, 4714–4727 (2014).
27. Y. Zhu, X. He, Y. Mo, Origin of outstanding stability in the lithium solid electrolyte materials: Insights from thermodynamic analyses based on first-principles calculations. *ACS Appl. Mater. Interfaces* **7**, 23685–23693 (2015).
28. Y. Zhu, X. He, Y. Mo, First principles study on electrochemical and chemical stability of the solid electrolyte-electrode interfaces in all-solid-state Li-ion batteries. *J. Mater. Chem. A* **4**, 3253–3266 (2015).
29. F. Han, Y. Zhu, X. He, Y. Mo, C. Wang, Electrochemical stability of $Li_{10}GeP_2S_{12}$ and $Li_7La_3Zr_2O_{12}$ solid electrolytes. *Adv. Energy Mater.* **6**, 1501590 (2016).
30. J. B. Bates, N. J. Dudney, G. R. Gruzalski, R. A. Zuhr, A. Choudhury, C. F. Luck, Electrical properties of amorphous lithium electrolyte thin films. *Solid State Ion.* **53–56**, 647–654 (1992).
31. T. Thompson, A. Sharafi, M. D. Johannes, A. Huq, J. L. Allen, J. Wolfenstine, J. Sakamoto, A tale of two sites: On defining the carrier concentration in garnet-based ionic conductors for advanced Li batteries. *Adv. Energy Mater.* **5**, 1500096 (2015).
32. L. Cheng, E. J. Crumlin, W. Chen, R. Qiao, H. Hou, S. Franz Lux, V. Zorba, R. Russo, R. Kostecki, Z. Liu, K. Persson, W. Yang, J. Cabana, T. Richardson, G. Chen, M. Doeff, The origin of high electrolyte-electrode interfacial resistances in lithium cells containing garnet type solid electrolytes. *Phys. Chem. Chem. Phys.* **16**, 18294–18300 (2014).
33. M. Kotobuki, H. Munakata, K. Kanamura, Y. Sato, T. Yoshida, Compatibility of $Li_7La_3Zr_2O_{12}$ solid electrolyte to all-solid-state battery using Li metal anode. *J. Electrochem. Soc.* **157**, A1076–A1079 (2010).
34. H. Buschmann, J. Dölle, S. Berendts, A. Kuhn, P. Bottke, M. Wilkening, P. Heitjans, A. Senyshyn, H. Ehrenberg, A. Lotnyk, V. Duppel, L. Kienle, J. Janek, Structure and dynamics of the fast lithium ion conductor "$Li_7La_3Zr_2O_{12}$". *Phys. Chem. Chem. Phys.* **13**, 19378–19392 (2011).
35. L. Cheng, W. Chen, M. Kunz, K. Persson, N. Tamura, G. Chen, M. Doeff, Effect of surface microstructure on electrochemical performance of garnet solid electrolytes. *ACS Appl. Mater. Interfaces* **7**, 2073–2081 (2015).
36. M. R. Busche, T. Drossel, T. Leichtweiss, D. A. Weber, M. Falk, M. Schneider, M.-L. Reich, H. Sommer, P. Adelhelm, J. Janek, Dynamic formation of a solid-liquid electrolyte interphase and its consequences for hybrid-battery concepts. *Nat. Chem.* **8**, 426–434 (2016).
37. X. Yu, Z. Bi, F. Zhao, A. Manthiram, Hybrid lithium–sulfur batteries with a solid electrolyte membrane and lithium polysulfide catholyte. *ACS Appl. Mater. Interfaces* **7**, 16625–16631 (2015).
38. F. Sagane, T. Abe, Y. Iriyama, Z. Ogumi, Li^+ and Na^+ transfer through interfaces between inorganic solid electrolytes and polymer or liquid electrolytes. *J. Power Sources* **146**, 749–752 (2005).
39. Y. Ishihara, K. Miyazaki, T. Fukutsuka, T. Abe, Kinetics of lithium-ion transfer at the interface between $Li_4Ti_5O_{12}$ thin films and organic electrolytes. *J. Phys. Chem. C* **3**, 83–86 (2014).
40. H. Kitaura, H. Zhou, All-solid-state lithium-oxygen battery with high safety in wide ambient temperature range. *Sci. Rep.* **5**, 13271 (2015).
41. L. Wang, Y. Wang, Y. Xia, A high performance lithium-ion sulfur battery based on a Li_2S cathode using a dual-phase electrolyte. *Energy Environ. Sci.* **8**, 1551–1558 (2015).
42. F. Sagane, T. Abe, Z. Ogumi, Li^+-ion transfer through the interface between Li^+-ion conductive ceramic electrolyte and Li^+-ion-concentrated propylene carbonate solution. *J. Phys. Chem. C* **113**, 20135–20138 (2009).
43. Q. Wang, J. Jin, X. Wu, G. Ma, J. Yang, Z. Wen, A shuttle effect free lithium sulfur battery based on a hybrid electrolyte. *Phys. Chem. Chem. Phys.* **16**, 21225–21229 (2014).
44. X. Yu, Z. Bi, F. Zhao, A. Manthiram, Polysulfide-shuttle control in lithium-sulfur batteries with a chemically/electrochemically compatible NaSICON-type solid electrolyte. *Adv. Energy Mater.* **6**, 1601392 (2016).
45. Y. Kihira, S. Ohta, H. Imagawa, T. Asaoka, Effect of simultaneous substitution of alkali earth metals and Nb in $Li_7La_3Zr_2O_{12}$ on lithium-ion conductivity. *ECS Electrochem. Lett.* **2**, A56–A59 (2013).
46. R. Murugan, V. Thangadurai, W. Weppner, Fast lithium ion conduction in garnet-type $Li_7La_3Zr_2O_{12}$. *Angew. Chem. Int. Ed.* **46**, 7778–7781 (2007).
47. Y. Li, Z. Wang, C. Li, Y. Cao, X. Guo, Densification and ionic-conduction improvement of lithium garnet solid electrolytes by flowing oxygen sintering. *J. Power Sources* **248**, 642–646 (2014).
48. M. M. Ahmad, M. M. Al-Quaimi, Origin of the enhanced Li^+ ionic conductivity in Gd^{+3} substituted $Li_{5+2x}La_3Nb_{2-x}Gd_xO_{12}$ lithium conducting garnets. *Phys. Chem. Chem. Phys.* **17**, 16007–16014 (2015).
49. A. Sharafi, H. M. Meyer, J. Nanda, J. Wolfenstine, J. Sakamoto, Characterizing the Li–$Li_7La_3Zr_2O_{12}$ interface stability and kinetics as a function of temperature and current density. *J. Power Sources* **302**, 135–139 (2016).
50. R. Kanno, M. Murayama, T. Inada, T. Kobayashi, K. Sakamoto, N. Sonoyama, A. Yamada, S. Kondo, A self-assembled breathing interface for all-solid-state ceramic lithium batteries. *Electrochem. Solid State Lett.* **7**, A455–A458 (2004).
51. J. van den Broek, S. Afyon, J. L. M. Rupp, Interface-engineered all-solid-state li-ion batteries based on garnet-type fast Li^+ conductors. *Adv. Energy Mater.* **6**, 1600736 (2016).

52. L. J. Miara, W. D. Richards, Y. E. Wang, G. Ceder, First-principles studies on cation dopants and electrolyte|cathode interphases for lithium garnets. *Chem. Mater.* **27**, 4040–4047 (2015).

53. A. Jain, S. Ping Ong, G. Hautier, W. Chen, W. Davidson Richards, S. Dacek, S. Cholia, D. Gunter, D. Skinner, G. Ceder, K. A. Persson, Commentary: The materials project: A materials genome approach to accelerating materials innovation. *APL Mater.* **1**, 11002 (2013).

54. S. P. Ong, L. Wang, B. Kang, G. Ceder, Li–Fe–P–O_2 phase diagram from first principles calculations. *Chem. Mater.* **20**, 1798–1807 (2008).